Detection and Characterization of Maneuvers Using a Global Radar Network

Michael Squires
LeoLabs
Nathan Griffith, James Rowland, Matthew Stevenson
LeoLabs

ABSTRACT

In this paper we describe a series of configurable algorithms to detect and characterize maneuvers in an automated fashion, and a corresponding series of analyses supporting their successful employ.

The first element in our automated detection and characterization algorithms is the configurable maneuver detector. The configuration options for the detector pertain to the number of tracklets (sets of coherent radar measurements) present in a detection window and signal hypothesis sensitivity. The tracklet window size setting varies the detection latency from low, using the first radar measurements past the putative maneuver event, to a high latency with a low false positive detection rate which uses more radar data. In both cases the sensitivity precludes any appreciable rate of false negatives. The low latency single tracklet detection window is especially useful for high interest objects where an elevated false positive detection rate is acceptable. The low false positive rate higher latency modes work best for passively monitoring a large catalog of objects where frequent alerts are undesirable. Both modes are demonstrated in this paper.

The configurable maneuver characterizer models maneuvers as impulsive, with adjustable fit regularization and fit bounds. These parameters allow one to search the solution space most likely to contain the correct post-maneuver object state. Successive widening of the bounds and disabling of regularization parameters allows the system to fit more unlikely varieties of maneuvers. The output of the maneuver characterizer includes an improved estimate of maneuver time and estimated impulsive velocity vector. Metrics from the fit, including quality of fit and magnitude of the maneuver can be utilized to veto any false positive detection. Additionally, we show that incorporating the estimated maneuver in a true positive case, allows the state produced by the nominal orbit determination system to quickly converge to the true state post maneuver.

We present a series of analyses applying these algorithms to LeoLabs radar data. We show validation against third party information including International Laser Ranging Service (ILRS) ephemeris with maneuver truth. We also show the application of the maneuver detector on known non-maneuverable objects of various classes to demonstrate low false alarm rate and apply our algorithms to an operational set of non-cooperative high interest objects, highlighting likely maneuvers based upon appreciable changes to object Keplerian orbital elements. The maneuver detection and characterization system is shown to perform well in all the studied cases.

1. THE GENERAL PROBLEM OF MANEUVER DETECTION AND CHARACTERIZATION

In the context of operational space missions, space situation awareness (SSA) is critical for operators in order to maintain a usable orbit and complete the mission as designed. Collisions or radio communications interference by other live missions may prevent successful completion. While collisions can occur with any resident space object, one key aspect of space situational awareness is monitoring the actions of other space missions which entails both the monitoring of those mission's nominal orbit and any orbit changes. Of these two elements, it is particularly challenging to monitor orbital changes induced by maneuvers. Detecting and characterizing any maneuvers that may be present in these missions is thus of paramount importance to the operator.

In this paper we describe a series of configurable algorithms to detect and characterize maneuvers. We will begin by describing our radar network, nominal data flow, and data processing. We will then describe the algorithms for maneuver detection and characterization, and their results with LeoLabs data, International Laser Ranging Service (ILRS) data, and 18th Space Defense Squadron two-line element sets (TLEs).

2. RADAR NETWORK AND NOMINAL DATA PROCESSING

The LeoLabs global radar network currently consists of ten phased array radars located at six sites, four of which are S-band radar instrument pairs. These sites are globally distributed, with coverage for resident space objects (RSO) down to 10cm in size to low equatorial inclination. Fig. 1 shows the current distribution of our radar network and a notional radar field of view (FOV). For more information on the radar network consult [5].
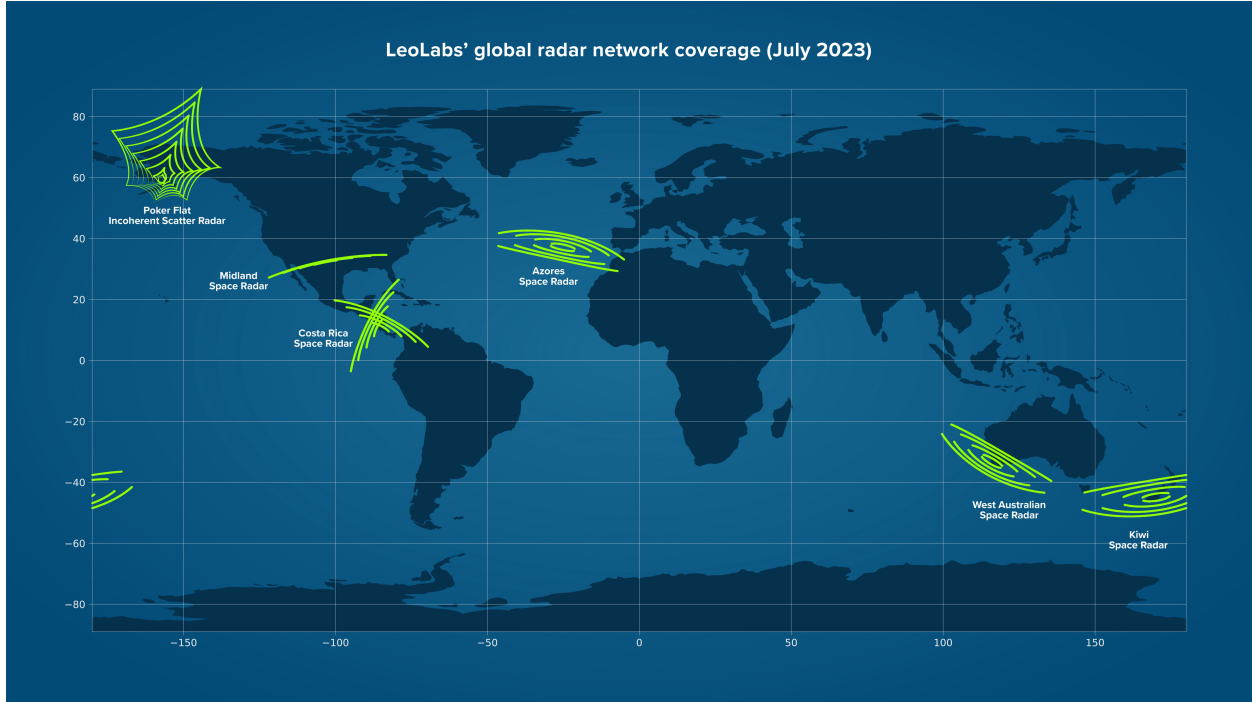

Fig. 1 - LeoLabs radar site distribution

The LeoLabs data used in this study originate from these radar stations. When a resident space object passes through a radar FOV, the radar collects a series of range and doppler measurements. The total collection of measurements, which may include other resident space objects, is called a radar pass.

In each radar pass measurements are then segmented into sets (which we denote as tracklets) of range and doppler pairs at each measurement time. The set of range-doppler pairs are then fit with a simple constant acceleration dynamical model valid for small time intervals given by the following equations:

$$\rho = \rho + \dot{\rho}t + 0.5\ddot{\rho}t^2$$

$$\dot{\rho} = \dot{\rho} + \ddot{\rho}t$$

For less common long duration tracklets in our system we fit to third order, the details of which we omit here. The fit values for range and doppler at the fit time are then used in a Bayesian likelihood measurement-to-object associator. This associator compares the predicted values for range and doppler at the tracklet fit time using the covariance of the object to assess distance in probability space and hence probability of association. This process is performed for all objects that could reasonably associate (i.e., pass certain timing and kinematic cuts) with the new tracklet. Associated tracklets are then passed into the orbit determination system (OD) along with the prior state of the matched object to begin the state update process.

The OD system utilizes an unscented Kalman filter (UKF) that models nominal, non-maneuvering, orbit dynamics when ingesting new measurements. The modeled forces consist of:

- 42 x 42 gravitational field model, JGM-3
- Solar 3rd body gravity
- Lunar 3rd body gravity
- Isotropic atmospheric drag (NRLMSISE-00 atmosphere model)
- Isotropic solar radiation pressure

The filter performs numerical propagation and measurement incorporation in conjunction with a state noise compensation algorithm (SNC). This algorithm models additional noise in the state, not captured by covariance propagation. Specifically, the SNC algorithm models error induced in the state by:

- Gravitational field truncation and uncertainty
- Drag and atmospheric uncertainty
- Solar radiation pressure (SRP) force uncertainty

After measurement incorporation the state is propagated backwards one day and forwards five days. A tracklet veto check is performed on the normalized measurement residuals. Tracklets incompatible with the state are rejected and a new state is not uploaded. A similar check is performed on the updated state Keplerian elements. Updates with very large changes to the state elements are rejected. Compatible updates are uploaded into the production system and the cycle repeats anew for each object with each new associated tracklet.

3. MANEUVER DETECTION ALGORITHM

For maneuver detection we begin with a simple hypothesis test; H_0 = No Maneuver, H_1 = Maneuver. We select as our test statistic, the estimated tracklet timing (radar-dt metric), which is a metric we use during launch support to gauge temporal positioning of objects released in a ride share. The radar-dt timing metric is as follows:

$$dt_{range} = \frac{\rho_t - \rho_s}{\dot{\rho}_t}$$

Equation 1 - radar-dt range timing metric

and,

$$dt_{doppler} = \frac{\dot{\rho}_t - \dot{\rho}_s}{\ddot{\rho}_t}$$

Equation 2 - radar-dt doppler timing metric

The range, range rate, and range acceleration are the fitted values as described in Section 2, as performed on the tracklet constituent measurements. The range, and range rate values with the "s" subscript are those predicted at the tracklet fit time by the state immediately prior to the tracklet under consideration. In the nominal situation, the dynamics of the RSO are well modeled by the OD system described in Section 2 and the time differentials in Equation 1 and Equation 2 are near zero. In the signal hypothesis case we expect significant timing divergence, which can indicate a maneuver has occurred. There are a few other possible causes for an elevated timing metric, namely: poorly modeled objects, false positive tracklets, or inappropriately associated tracklets. In order to suppress the error rate induced by these alternative causes we first examine the distributions of the radar-dt metric on RSOs that cannot maneuver.

In Fig. 2 we examine 200 debris targets over 8 days of collection to yield $\mu_r = 0.0138$ seconds and $\sigma_r = 0.7170$ seconds in range-dt, and $\mu_{\dot{r}} = 0.0445$ seconds and $\sigma_{\dot{r}} = 0.2052$ seconds in doppler dt. In Fig. 3 we examine this same metric for 300 rocket bodies collected over 8 days and we get: $\mu_r = 0.0102$ seconds and $\sigma_r = 1.285$ seconds in range dt, and $\mu_{\dot{r}} = 0.0601$ seconds and $\sigma_{\dot{r}} = 1.552$ seconds in doppler-dt. We notice that the radar-dt sample standard deviations are elevated over those found in the debris sample. This could possibly be due to rocket body out gassing and attitude changes due to uncontrolled tumbling. In Fig. 4 we show this same set of metrics for targets

that maneuver during times in which they are active. There is a clear separation in timing between this data and the nominal, non-maneuverable targets which shows the metric's suitability for use in a detector. Accordingly, these sample standard deviations will be used to compute our likelihood values for detection which conform to the hypothesis stated at the beginning of this section. In Section 5, Results, we show efficient values for σ_r and $\sigma_{\dot{r}}$ empirically calculated by tuning against maneuvers found in ILRS data.
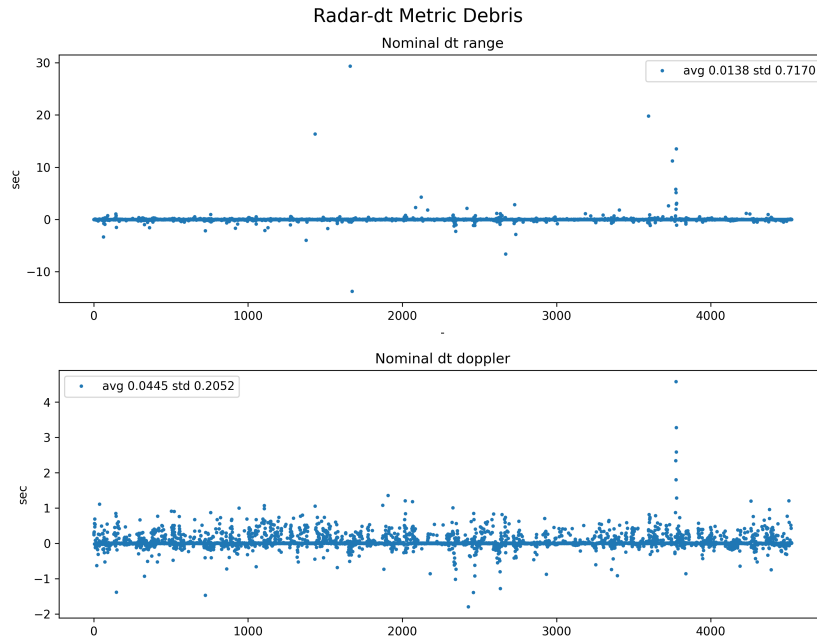

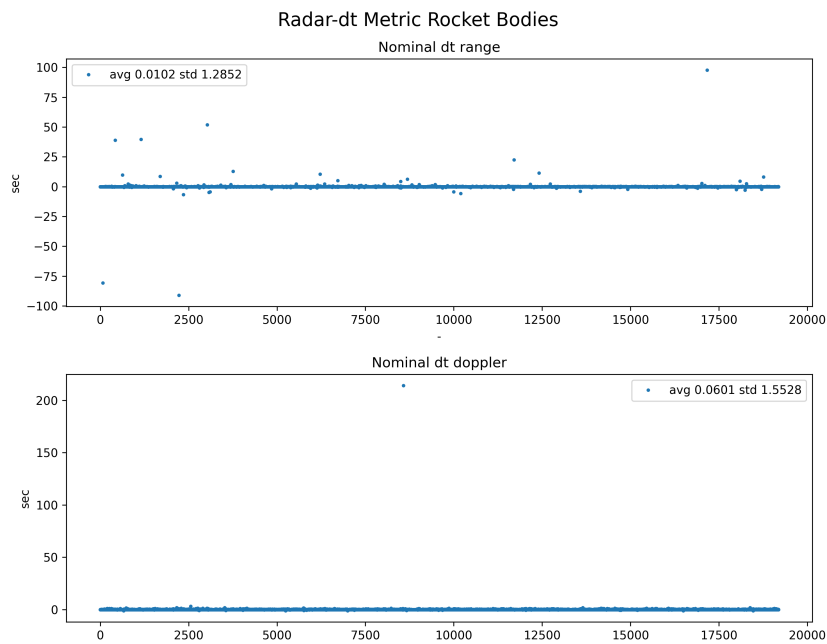*Fig. 2 - The radar-dt timing metric on 200 debris objects*

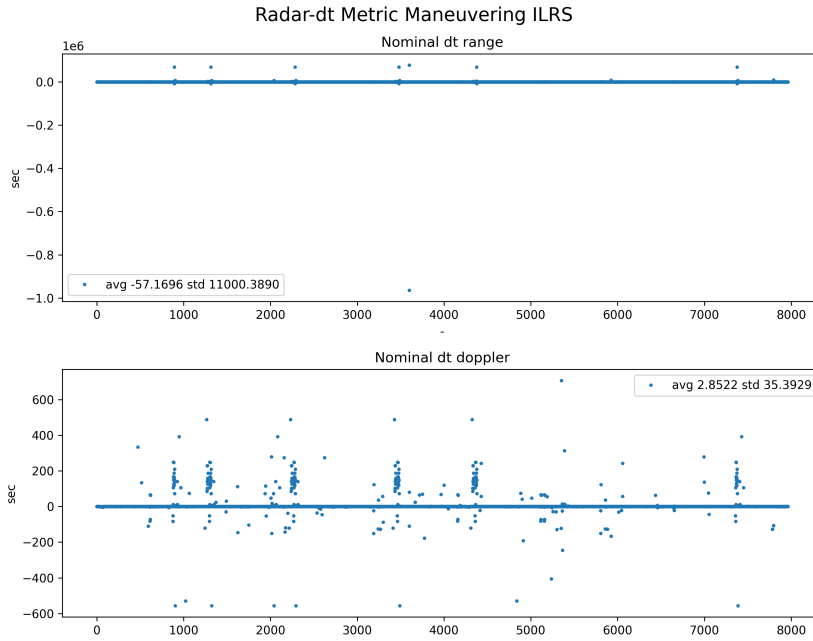*Fig. 3 - The radar-dt timing metric on 300 rocket bodies*

Fig. 4 - The radar-dt metric on maneuvering ILRS objects. A clear outlier is seen in range-dt.

By using the sample standard deviations (or tuned values) on these metrics, we can combine range and doppler timing metrics into a single value by employing a likelihood formulation with the following form:

$$p_{MD} = e^{-\frac{1}{2}(MD)^2}$$

Equation 3 - Mahalanobis likelihood

Where MD is the Mahalanobis distance formulated with the appropriate sample (or computed) covariance values. In order to suppress false alarms in the presence of the tracklet association error sources we described earlier, we allow for the detector to vary the number of tracklets used in the hypothesis test- the greater the number of tracklets used the less likely we are to detect based on a false association or tracklet. For a single tracklet the likelihood function used is shown in Equation 3. For two and three tracklet windows we use the following formulae representing the likelihood that any of the tracklets (events) in the window are nominally displaced in time:

$$\mathcal{L} = p_1 + p_2 - p_1 p_2$$

$$\mathcal{L} = p_1 + p_2 + p_3 - p_1 p_2 - p_1 p_3 - p_2 p_3 + p_1 p_2 p_3$$

Where the subscript number represents the ith tracklet in the detection window and the "p" represents that tracklet's p_{MD}. These equations will have a value approaching 1.0 if all the constituent tracklets in the detection window have small radar-dt metrics. Each detection window is thus mapped to a single likelihood value no matter how many tracklets compose the window. We can then signal a detection when this likelihood drops below a signal threshold value which can be set based on the desired delta-v sensitivity and false alarm rate.

Once a detection has been signaled, the likelihood values will remain low, and possibly trigger additional detections for a period of time. This period of low likelihoods is the refractory period, which is proportional to the magnitude of the maneuver's delta-v and is a result of Kalman filter lag. We therefore introduce a stabilization requirement to the detector wherein the likelihood values must return to nominal for a minimum number of consecutive detection windows before the detector is allowed to detect maneuvers again. This value is configurable. In Fig. 5 we

demonstrate the aforementioned detector characteristics including refractory period. The output maneuver date is set as the time halfway between the prior state's epoch and first tracklet in the detection window.

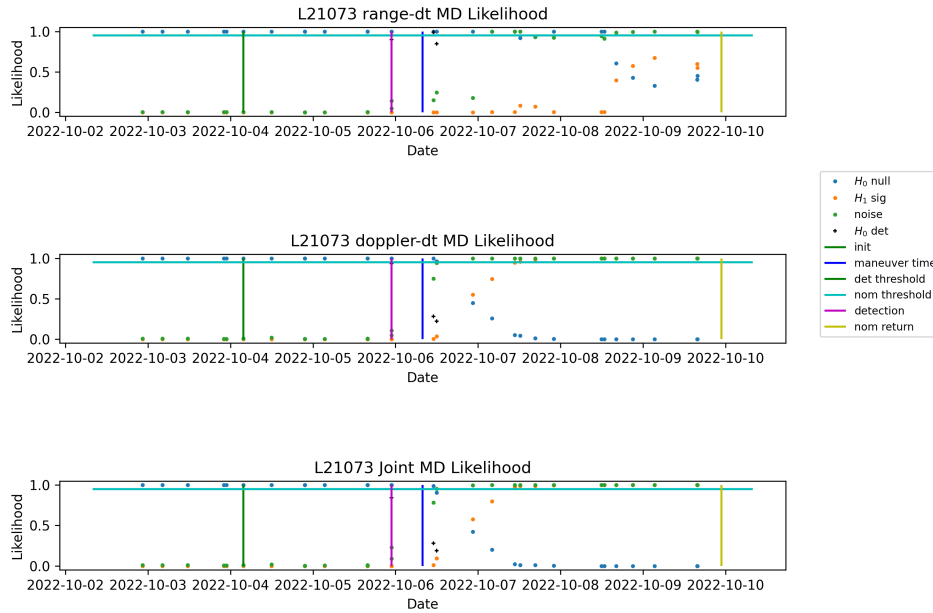Detections- Window Size 3 - True $\Delta v =$ 2.136 m/s

Fig. 5 - Detection on an ILRS target with a real maneuver. The real maneuver is represented by the blue line. The detection and nominal threshold horizontal lines coincide in this detection parameter set.

4. MANEUVER CHARACTERIZATION ALGORITHM

After maneuver detection, the task becomes estimating the size and more precise timing of the maneuver. For this task we turn to the input estimation technique (this entails estimating the input to the nominal state required to better fit the collected data based on an alternative dynamics model) where we take the maneuver detector output, $S_{prior}, t_1, t_2, t_3, \ldots$ (where S_{prior} represents the prior state and t_i represents the ith tracklet in the detection window) and use constrained fitting in order to estimate the input to the state, i.e. the maneuver, required to fit the tracklets. We begin by assuming a simple single impulsive maneuver that occurs outside the tracklet measurement windows, between the prior state, S_{prior} and t_1. This is a reasonable assumption as the typical tracklet time duration in the LeoLabs radar network is on the order of a few seconds, which is small compared to the duration between tracklet collection which is on the order of a few minutes to a few hours.

By assuming that the maneuver was completed before tracklet collection, the space object will be in a new orbit at tracklet collection times in the detection window. This new orbit can be represented by the state, S'. We begin by fitting this new orbit with a constrained global-local minimizer. The initial state is the prior state, S_{prior} and the fit constraint is minimized delta-v between S_{prior} and S' at each tracklet fit point ($min\Sigma|dV|$). The S' orbit is also constrained (initially) to being elliptical. The fitter then proceeds to loop between the constrained least-squares and a Nelder-Mead simplex minimizer. Widening of the fitter parameter bounds, and elimination of the fit constraint occurs in each successive fitter loop. The algorithm stays in this loop until fit quality conditions are met or the maximum allowable number of fit loops have been performed (this is set to three).

If a new orbit has been fit at a satisfactory reduced $\chi^2 < 100.0$ - 150.0 we then find the point of closest approach (PCA) between S' and S_{prior}. At the PCA we can then compute the delta velocity of S' in the RSW reference frame of the prior orbit. The time of the PCA and delta-v in RSW is then reported as the maneuver time and delta-v.

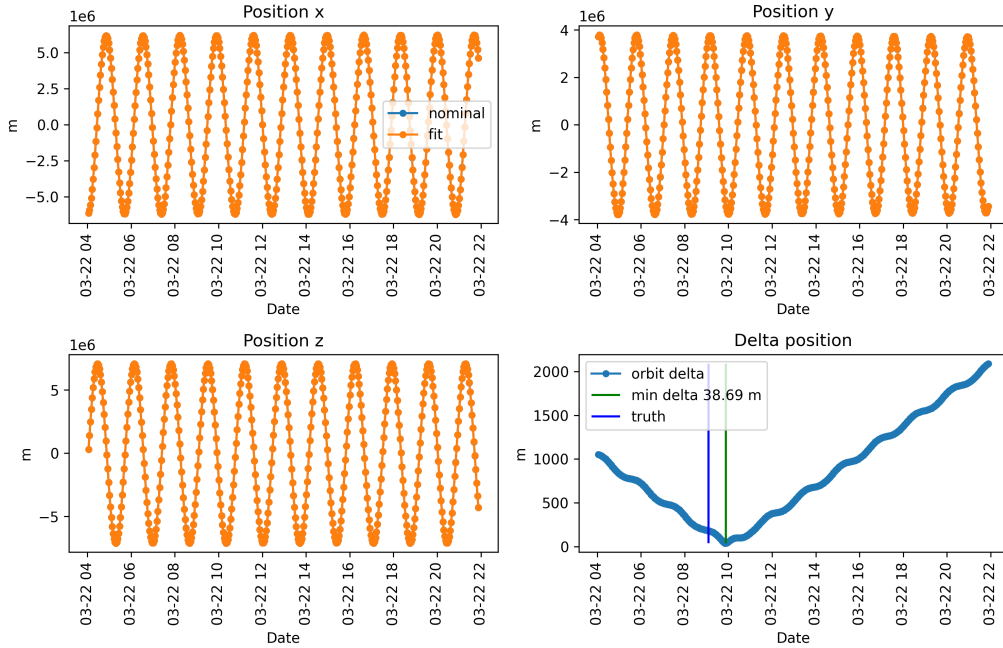X,Y,Z and |D| of S, S' from 03/22/2023 04:03 to 03/22/2023 21:54

Fig. 6 - Positions x, y, z in EME 2000 for target L21073. The lower right plot is the delta position with minimum denoted by the green line. The true maneuver time is denoted by the blue vertical line.

5. RESULTS

The external data we use to examine performance of maneuver detection and characterization algorithms originate from the ILRS (International Laser Ranging Service) and the 18th Space Defense Squadron. We begin by outlining the datasets and targets used for algorithm assessment.

Table 1 - Data sets

Targets	Data	Data Set Types	Date Range
Debris	200 objects with 8 days of collection	TLEs, States, Tracklets	6/10 – 6/18 2023
Rocket Bodies	300 objects with 8 days of collection	TLEs, States, Tracklets	6/1 – 6/9 2023
Maneuvering ILRS Objects (Payloads)	102 Maneuvers over 5 objects	TLEs, States, Tracklets, ILRS maneuver files	1/1/2022 – 5/3/2023
High Interest Objects (Payloads)	53 objects over 8 days of collection	TLEs, States, Tracklets	6/1 – 6/9 2023

For the maneuver detector we scan in detector parameter space and plot the false positive rate vs true positive rate for tracklet detection widths of 1-3. Fig. 7 shows this performance curve with Pareto front. The data used are "Maneuvering ILRS Objects" and "Rocket Bodies". The "Maneuvering ILRS Objects" give us a source of true positive maneuvers and the rocket bodies give us a source of false positives.

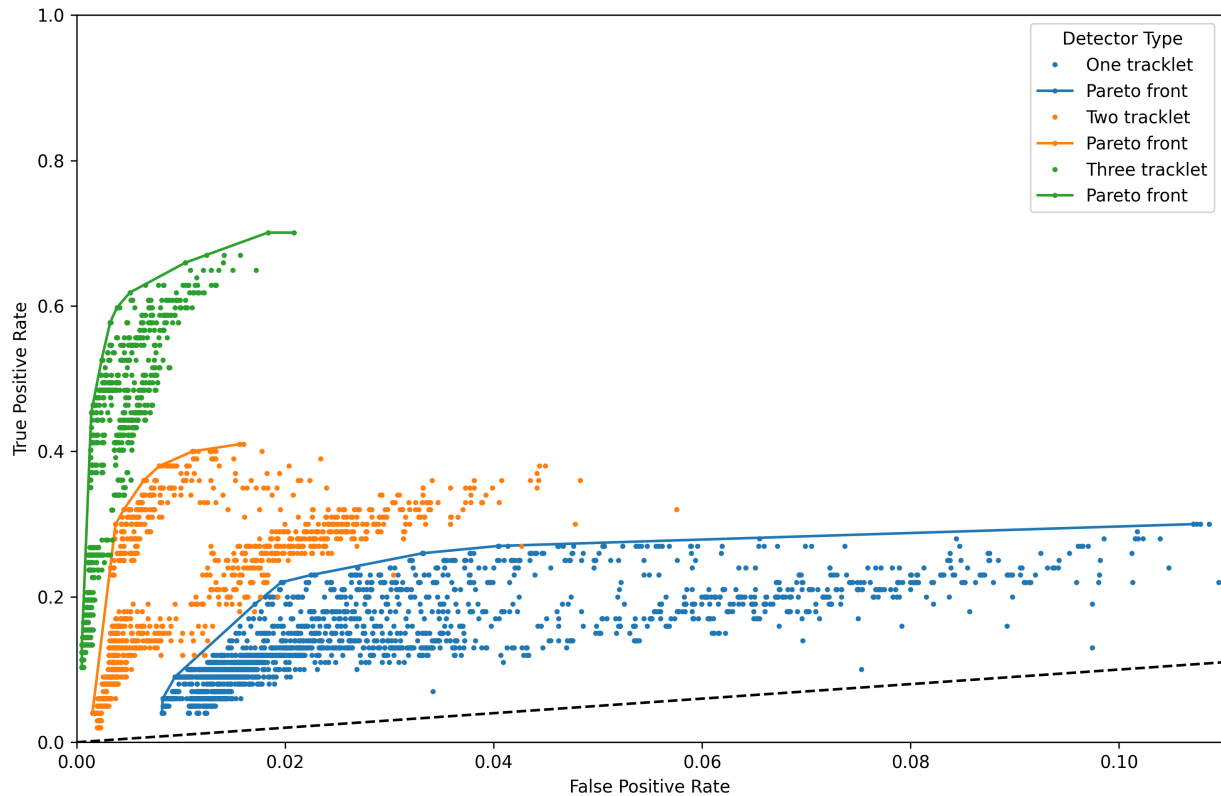ROC Curves for Maneuver Detection

Fig. 7 - Receiver operating characteristic curve with Pareto front

We see that we achieve a very low false alarm rate in all cases on the Pareto front and we primarily miss maneuvers with small delta-v, which is the bulk of the data set. Approximately 20% of the maneuvers are above 0.1 m/s delta-v of which all detection windows perform well on. For smaller detection windows (window size < 3) there are two primary sources of missed detections. The first of which is detection lag, where the detection occurs later than the actual maneuver and is counted as a false positive and a false negative as opposed to a true positive detection. We propose a solution to this scenario in Section 6. The second source is false positive tracklet or incorrect object-to-tracklet association which causes the algorithm to trigger a detection before the actual maneuver. The real maneuver will thus lie within the refractory period of the false positive and is labeled as a false negative. This defect can be remedied by improvements to the Bayesian object-to-measurement associator.

Now we move on to exploring the high interest object (HIO) set via hand labeling maneuvers with third party data (see Appendix A) and comparing to our detector running a chosen parameter set.

The high interest object data set consists of 53 objects observed over a randomly selected period of 8 days, starting June 1, 2023 to June 9, 2023. These objects consist of known and suspected maneuverable payloads that engage in atypical behavior with respect to other payloads. One such example in this dataset is Cosmos 2542, which has been reported to track US government assets [9]. Since targets such as these are of interest to the SSA community we compare our detector and analyst driven TLE element change detection on 18th Space Defense Squadron TLE data. The detector parameters we chose are: $\sigma_\rho = 0.1$ seconds, $\sigma_{\dot{\rho}} = 1.6$ seconds, and likelihood crossing threshold = 0.25 with a reported true positive rate of 77% and a reported false positive rate of .06% on maneuvers in ILRS with dv > 0.1 m/s. The results are showcased in Table 6 (see Appendix B) and Table 2.

Table 2 - Hand labeling to maneuver detector confusion matrix. Results are per-target.

		Maneuver Detector	
		Detection	No Detection
	Detection	4	1
Hand Labeling	No Detection	8	40

With our chosen data point we achieve reasonable performance- with only one missed detection. Several targets in the false-positive category are very poorly tracked and result in multiple false positive detections (which can also be seen in the characterization results). These poorly tracked (and/or modeled) objects explain why the false positive rate is higher than the quoted rate from well-tracked ILRS targets.

With the results from our detector elucidated we move on to exploring the characterizer algorithm's performance. Using ILRS maneuver truth described in Table 1 we run the characterizer on a window of four tracklets to yield the following:
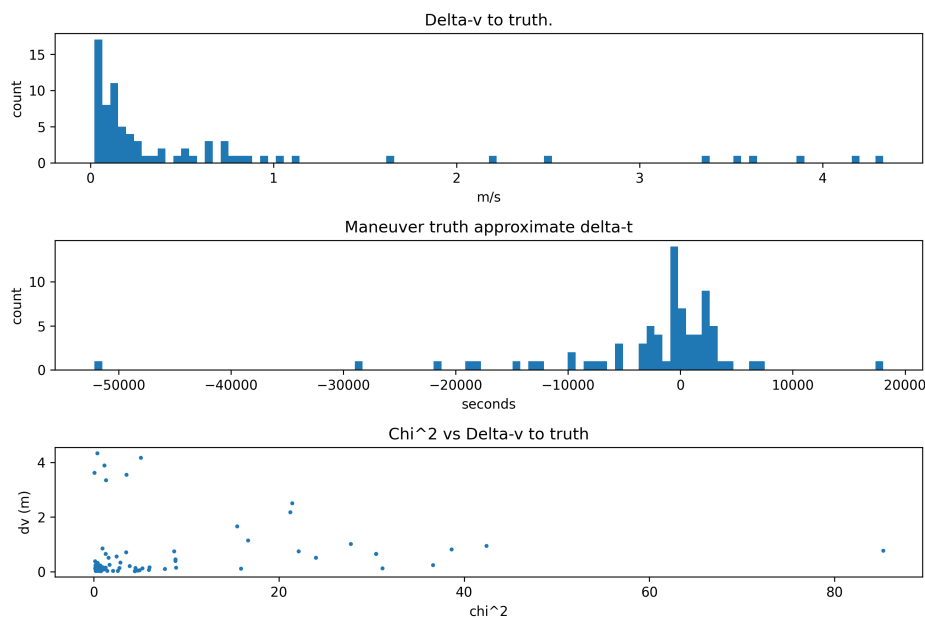
Characterizer Truth Ensemble on 77 Maneuvers

Fig. 8 - Characterizer truth on 102 ILRS maneuvers passing cuts

We lose 25 maneuvers due to missing LeoLabs data or failing the loose reduced χ^2 cut on the fit quality of the S'
orbit. The maneuvers shown produce fit delta-v to true delta-v values according to the following table:

Table 3 - Delta-v magnitude from true delta-v (m/s)

50th percentile	75th percentile	90th percentile	Max
0.15	0.65	1.86	4.33

And the estimated time of the maneuver falls within:

Table 4 – Delta-t (minutes) from estimated maneuver date to actual maneuver date

50th percentile	75th percentile	90th percentile	Max
38	70	214	869

Applying the same maneuver delta-v estimation technique to 18th TLEs (sans S' state fitting as we have a TLE prior
and posterior to the maneuver; we use the TLE for PCA and delta-v finding) for the same maneuvering ILRS targets
we arrive at the results shown in Fig. 9.
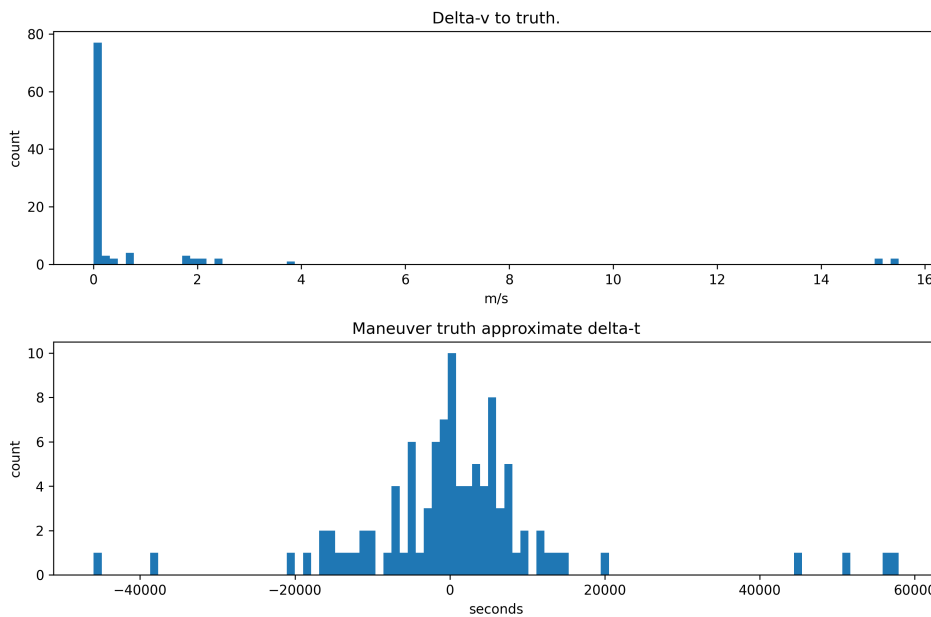
Characterizer Truth Ensemble on 100 Maneuvers

Fig. 9 - Delta-v characterization on 18th TLE data

When using the TLE data from the 18th Space Defense Squadron we see that the delta-v to true delta-v distance and
time distance distributions are narrow, but with longer tails. We also note that the number of objects that can be fit

are greater. These results demonstrate that the maneuver PCA and delta-v portion of the characterization algorithm perform comparably with an alternative S and S' data source.

With the HIO object collection we perform a three tracklet fit to the detected maneuvers. In Table 5 the results are shown. We perform a loose reduced χ^2 cut on the data of 150. Most of the false positive detections (e.g., XJS F) have small reduced χ^2 and low maneuver delta-vs. These correspond to states just far away enough from nominal radar-dt metrics to trip the detector and signal the characterizer to perform a fit. Very good fits with very small delta-vs tend to indicate false positive detections, as opposed to real maneuvers. Finally, we note that in the case of three or fewer tracklets in the fit window we are subject to large variations in fit delta-v with loose (above 100) reduced χ^2. We thus recommend < 100 for 3 tracklet characterizations and < 100 – 300 for four tracklet and larger fit windows.

Table 5 - High Interest Object Maneuver Characterization (3 tracklets) passing loose cuts. Asterix denotes objects above optimal 100 reduced chi squared cut.

LeoLabs ID	NORAD ID	Name	Country	Est. Maneuver Date	dv magnitude	χ^2
L7775280	48274	CSS (TIANHE-1)	CN	2023-06-05 16:51:06.999633	0.754671144	18.71908248
L319475	45249	XJS C	CN	2023-06-04 23:16:14.326341	0.882046405	8.360305076
L326813	45253	XJS F	CN	2023-06-02 06:09:00.278678	0.09514274	3.719003032
L326813	45253	XJS F	CN	2023-06-03 01:25:34.531503	0.5116778	6.672724724
L326813	45253	XJS F	CN	2023-06-05 23:03:32.564476	0.414868883	3.814101728
L326813	45253	XJS F	CN	2023-06-06 18:44:33.851132	0.184664671	7.846607717
L326813	45253	XJS F	CN	2023-06-07 23:53:15.615058	0.995743687	6.703536595
L2757731	45612	XJS H	CN	2023-06-03 00:39:40.448326	0.869940291	11.46198668
L2757731	45612	XJS H	CN	2023-06-06 18:01:39.784549	0.334095291	7.665419197
L21371	43518	XJS A	CN	2023-06-03 22:57:05.273738	0.257850021	4.110434049
L326811	45251	XJS E	CN	2023-06-02 23:18:08.213325	0.142209473	6.038662199
L326811	45251	XJS E	CN	2023-06-05 23:24:22.994540	0.187074911	4.169066722

L326811	45251	XJS E	CN	2023-06-06 17:28:54.296236	0.621757811	4.171360197
L4194268	45915	OBJECT E	RU	2023-06-05 05:43:34.805371	1.397396075	7.929468258
L131324	53370	KHAYYAM	IR	2023-06-03 06:17:15.910289	1.815432942	1.785924154
L131324	53370	KHAYYAM	IR	2023-06-06 12:34:29.515555	2.572890772	39.29023143
L7773986	47546	COSMOS 2549	RU	2023-06-05 00:00:35.481596	0.837701737	117.2159361*
L7775061	48157	SHIYAN 6 03 (SY-6 03)	CN	2023-06-06 15:28:49.962845	101.5221039	106.139085*

A challenge to the detector, as outlined in Section 3 and shown in Fig. 5, is that the nominal Kalman filter state lags the true state when a maneuver is performed. Given the characterizer more closely models the true dynamics of the resident space object we demonstrate that incorporating a good estimate (an estimate passing the reduced χ^2 cut) reduces the size of the tracklet residuals/filter innovations. This correspondingly reduces the required refractory period and hence increases the speed at which the detector can detect additional maneuvers. Fig. 10 compares measurement incorporation under nominal non-maneuvering dynamics in two cases: "fit" where the estimated maneuver was incorporated into the state and "nominal" where the filter operates as it normally does. Despite a sub-optimal fit in the demonstrated case, the residuals are smaller in the fit case which would result in correspondingly smaller radar-dt metrics.

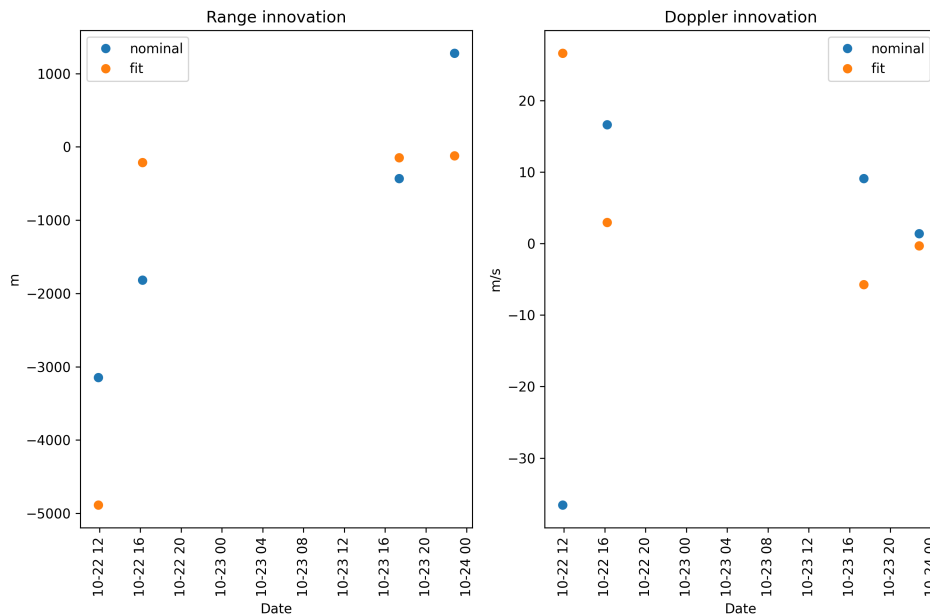Innovations for 4 Tracklets Post Maneuver Window

Fig. 10 – Innovations compared for nominal (blue) to state with fit maneuver (orange) for the four tracklets post characterization window.

Finally, we demonstrate the results of the combined maneuver detector and characterizer on the HIO targets in a prototype user GUI in Fig. 11.
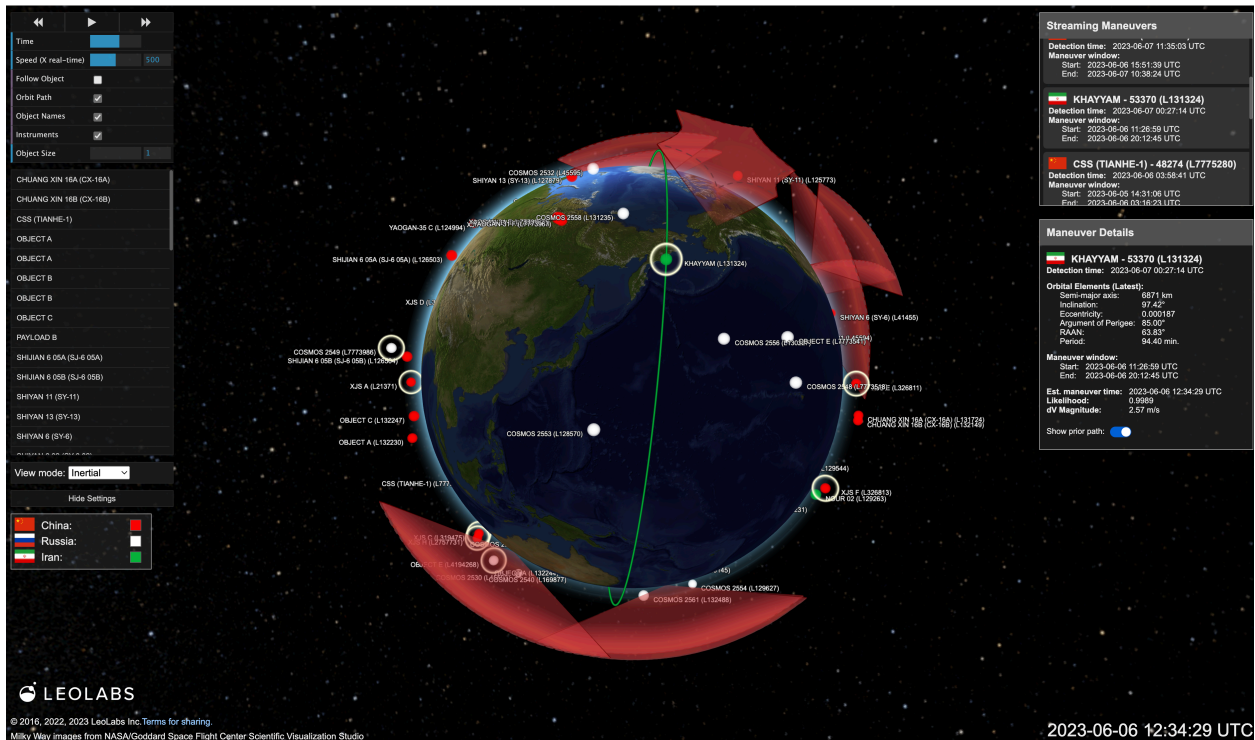

Fig. 11 - Prototype GUI combining maneuver detection and characterization show for the HIO target data set

The goal of this particular view of our system is to quickly display targets in a target set, over a desired date range (or in real-time), with the targets likely to have maneuvered in the upper right. Upon selecting a maneuvering target, the user would then be presented the estimated maneuver magnitude and time. Users can then look at the orbit at that time and inspect the orbit before and after the maneuver. This view furnishes the analyst/user with a complete high-level display of the situation involving all targets in the set.

6. EXTENSIONS AND FUTURE WORK

We now outline several avenues for improvement of the described algorithms and a few words on improvements to the nominal data processing chain that would improve performance. For the detector, improved underlying measurement-to-object association would have a large impact. This is particularly evident for smaller tracklet detection widths in which one incorrect association can result in a false alarm. Another issue with data input to the detector is if a maneuver is large enough in magnitude the underlying Bayesian object-to-measurement associator can label new measurements as not associated with the correct maneuvering target. This scenario would then result in no new tracklets for the maneuver detector to operate on.

In Fig. 4 we see an unphysical large range-dt metric; these can be filtered in the algorithm directly by setting a maximal time cut on both the range and doppler radar-dt metrics. We also note that some RSOs are very stable and well-tracked, whereas others have rather noisy (state inaccuracies) data. Thus, target specific dt metric sigmas would improve the quality of the detector.

Another direct improvement to the detector (and base system) would be to begin incorporating maneuver estimates into the state as described in Section 5. This would directly reduce the detector refractory period and allow for rapid detection of additional maneuvers, in addition to creating superior quality states.

In contrast to the detector and the object-to-measurement associator, the characterizer does not use the tracklet acceleration when fitting the post maneuver S' orbit. Given that the fitted tracklet acceleration further constrains the fit, it is logical to add tracklet acceleration to the fitter. Occasionally, for larger tracklet detection windows, the first tracklet in the window may be before the actual maneuver. In this case it would be beneficial to exclude this tracklet from any fit. To improve this, we would pass along each tracklet's detection likelihood and remove tracklets that associate well with the prior state from the fit.

In addition to the listed algorithm improvements, future work involves studying different classes of maneuvers and propulsion types, including long duration, low thrust maneuvers. We also plan to study larger detection windows and a larger parameter space for the adjustable detector settings.

The set of algorithms described provide an excellent basis for rapid detection and characterization of maneuvers with a highly extensible and modifiable platform for future improvements.

7. ACKNOWLEDGEMENTS

8. REFERENCES

[1] Byron Tapley, Bob Schutz, and George Born. *Statistical Orbit Determination*, Elsevier Academic Press, 2004.

[2] David Vallado. *Fundamental of Astrodynamics and Applications 5th Edition*, Space Technology Library, 2022.

[3] Yaakov Bar-Shalom, X. Rong Li, T. Kirubarajan. *Estimation with Applications to Tracking and Navigation*, John Wiley and Sons, Inc., 2001.

[4] James Wertz, David Everett, and Jeffery Puschell. *Space Mission Engineering: The New SMAD*, Space Technology Library, 2011.

[5] James Rowland, et al. A Worldwide Network of Radars for Space Domain Awareness in Low Earth Orbit, *AMOS Conference Proceedings*, 2021.

[6] M.R. Pearlman, C.E. Noll, E.C Pavlis, et al. The ILRS: approaching 20 years and planning for the future. *J Geod* 93, 2161–2180 (2019). DOI: https://doi.org/10.1007/s00190-019-01241-1.

[7] 18th Space Defense Squadron, Two Line Element Sets, 2023.

[8] C. Truong, L. Oudre, N. Vayatis. Selective review of offline change point detection methods. *Signal Processing*, 167:107299, 2020.

[9] W.J. Hennigan, Exclusive: Strange Russian Spacecraft Shadowing U.S. Spy Satellite, General Says, https://time.com/5779315/russian-spacecraft-spy-satellite-space-force/, *Time Magazine*, Accessed July 28, 2023.

APPENDIX A – HAND LABELING

The typical task for hand labeling maneuvers involves an analyst examining appreciable and rapid changes to Keplerian orbital elements that normally evolve slowly over time. In order to examine the performance of our maneuver detection and characterization system on targets without maneuver truth data we hand-label probable maneuvers based on the above description with third party data (18th TLEs). Prior to labeling the HIO target set we

examined Keplerian orbital elements from 18th TLEs on targets with maneuver truth, and on non-maneuvering targets. We then set a labeling technique in advance of the analyst examining HIO targets. This technique is as follows:

- Inspect semi-major axis and inclination
- Element change must be abrupt and show a discontinuity
- Element change must persist for at least 3 subsequent orbital element data points

The plots examined by the analysts are as shown in Fig. 12.

L1159 Detections- Window Size 1
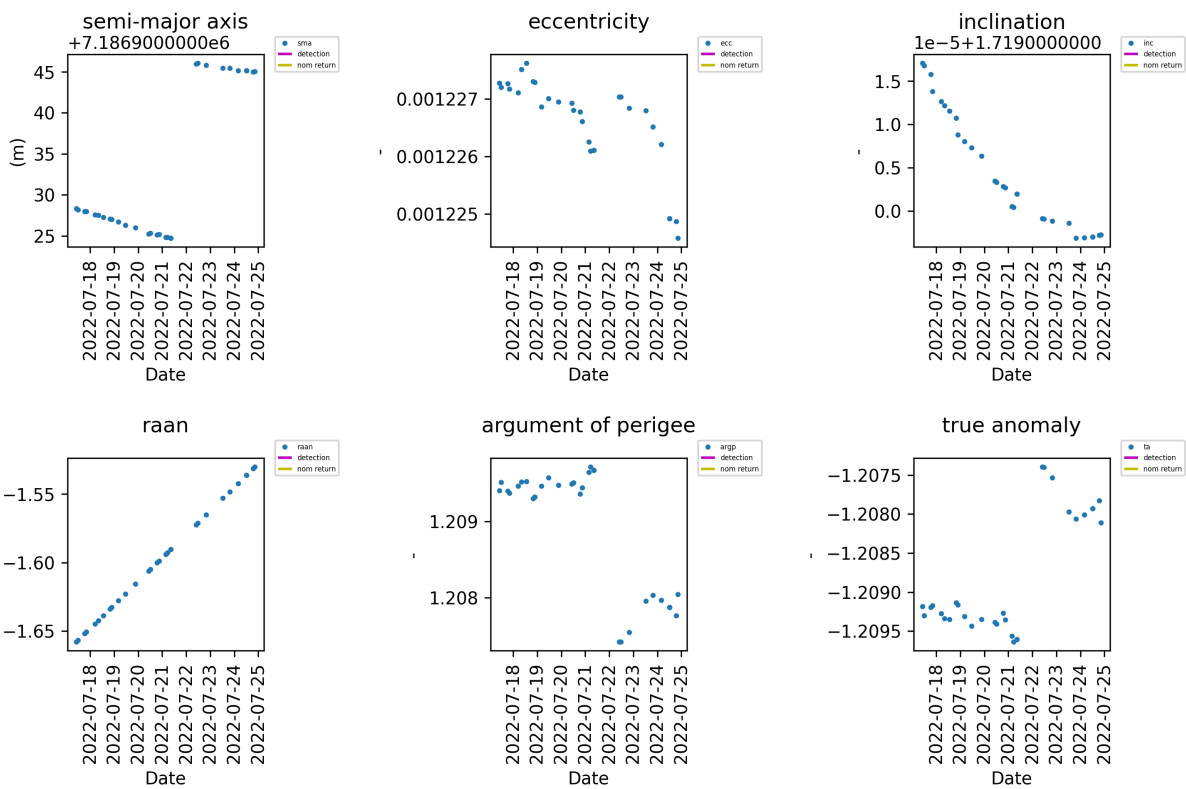
Fig. 12 - 18th TLE Keplerian Orbital Elements – data with a true maneuver shown at the break in semi-major axis.

APPENDIX B – HIGH INTEREST TARGET SET AND DETECTION LABELS

Table 6 - High Interest Object Collection and Detections

LeoLabs ID	NORAD ID	Name	Country	Detections	Manual Detections
L132231	53885	OBJECT B	CN	0	0
L132149	53876	CHUANG XIN 16B (CX-16B)	CN	0	0

L326813	45253	XJS F	CN	5	0
L131724	53586	CHUANG XIN 16A (CX-16A)	CN	0	0
L7773967	47536	YAOGAN-31 F	CN	0	0
L316376	45250	XJS D	CN	0	0
L41455	43711	SHIYAN 6 (SY-6)	CN	0	1
L132489	54110	COSMOS 2562	RU	1	0
L127879	51102	SHIYAN 13 (SY-13)	CN	0	0
L129263	51954	NOUR 02	IR	0	0
L326811	45251	XJS E	CN	3	0
L7773964	47533	YAOGAN-31 E	CN	0	0
L145939	44424	COSMOS 2538	RU	0	0
L21371	43518	XJS A	CN	1	0
L1304	41386	RESURS P3	RU	0	0
L132244	53948	OBJECT A	CN	0	0
L45593	43751	COSMOS 2530	RU	0	0
L2749006	45611	XJS G	CN	1	0
L3849145	45859	SHIYAN 6 02 (SY-6 02)	CN	0	0
L129544	52150	TK-2	CN	0	0
L130227	52713	COSMOS 2556	RU	0	0
L7773963	47532	YAOGAN-31 D	CN	0	0
L132246	53949	OBJECT B	CN	0	0
L4194268	45915	OBJECT E	RU	1	0
L128570	51511	COSMOS 2553	RU	0	0
L125773	49501	SHIYAN 11 (SY-11)	CN	0	0
L131235	53323	COSMOS 2558	RU	0	0
L124991	49390	YAOGAN-35 A	CN	0	0
L124994	49393	YAOGAN-35 C	CN	0	0
L7775280	48274	CSS (TIANHE-1)	CN	1	1
L2757731	45612	XJS H	CN	2	0
L7773541	47252	OBJECT E	RU	0	0
L124497	49113	PAYLOAD B	CN	0	0
L200176	44835	COSMOS 2543	RU	0	0
L45594	43752	COSMOS 2531	RU	0	0
L126504	49962	SHIJIAN 6 05B (SJ-6 05B)	CN	0	0
L124992	49391	YAOGAN-35 B	CN	0	0
L319475	45249	XJS C	CN	2	0
L129627	52202	COSMOS 2554	RU	0	0
L7773986	47546	COSMOS 2549	RU	1	1

L32629	43657	COSMOS 2528	RU	0	0
L45595	43753	COSMOS 2532	RU	0	0
L7775061	48157	SHIYAN 6 03 (SY-6 03)	CN	1	1
L145936	44421	COSMOS 2535	RU	0	0
L132230	53884	OBJECT A	CN	0	0
L132488	54109	COSMOS 2561	RU	0	0
L195057	44797	COSMOS 2542	RU	0	0
L21372	43519	XJS B	CN	0	0
L132247	53950	OBJECT C	CN	0	0
L7773518	47230	COSMOS 2548	RU	0	0
L131324	53370	KHAYYAM	IR	2	1
L169877	44517	COSMOS 2540	RU	0	0
L126503	49961	SHIJIAN 6 05A (SJ-6 05A)	CN	0	0